Contribution of ice dynamics along Nares Strait to the stability of ice arches

G.W.K. Moore

gwk.moore@utoronto.ca

University of Toronto

Stephen Howell

Environment Canada

Thomas Ballinger

University of Alaska Fairbanks

Kaitlin McNeil

University of Toronto

Mike Brady

Environment and Climate Change Canada

Article

Keywords: Ice Arches, Export of Arctic sea ice, ice dynamics, Nares Strait

Posted Date: March 8th, 2024

DOI: https://doi.org/10.21203/rs.3.rs-3976407/v1

Additional Declarations: No competing interests reported.

Contribution of ice dynamics along Nares Strait to the stability of ice arches

G.W.K. Moore[1,2]*, S.E.L. Howell[3], T.J. Ballinger[4], K. McNeil[1,2], M. Brady[3]

[1] Department of Physics, University of Toronto

[2] Department of Chemical and Physical Sciences, University of Toronto Mississauga

[3] Climate Research Division, Environment and Climate Change Canada

[4] International Arctic Research Center, University of Alaska Fairbanks

Manuscript submitted to *Scientific Reports*

February 21, 2024

**corresponding author:* gwk.moore@utoronto.ca

ABSTRACT

Nares Strait, situated between northwest Greenland and Ellesmere Island, is an important conduit for exporting sea ice from the Arctic, especially thick multi-year ice undergoing an accelerated loss compared to other ice types. This export is impacted by ice arches that can form along the Strait and remain stable for months at a time resulting in a reduction in ice export. Arch stability is a function of sea ice thickness and there is a concern that the thinning of Arctic sea ice may weaken the arches resulting in an accelerated export of sea ice. However, little is known about the spatial and temporal variability of sea ice thickness along the Strait. Here we show that before arch formation, there is a local maximum in ice thickness where arches typically form, which is related to ice convergence. Furthermore, we demonstrate that ice motion continues north of the arch after it forms, resulting in convergence and a dynamic thickening of the sea ice. We propose that, even though thinning ice is a cause for concern, the dynamics of sea ice transport along Nares Strait lead to localized thickening of sea ice that may contribute to continued arch formation and stability.

KEYWORDS

Ice Arches, Export of Arctic sea ice, ice dynamics, Nares Strait

INTRODUCTION

Nares Strait is the waterway that separates Greenland from Ellesmere Island (Figure 1). Along with Fram Strait to the east of Greenland and the Canadian Arctic Archipelago to the west of Ellesmere Island, the Strait is the major pathway along which sea ice leaves the Arctic Ocean[1-4]. The Strait is also a major pathway along which freshwater is exchanged between the Arctic and North Atlantic Oceans[5]. The Arctic's oldest and thickest sea ice is directly north of Nares Strait[6] and has seen an accelerated loss in recent years[7]. Much of the export of this multi-year ice-class occurs along Nares Strait[8], and there has been a recent increase in ice transport along the Strait [1,2].

Ice arches typically form along the Strait in early winter, i.e., November-January, and can remain stable until the early summer, i.e., June-July[9,10]. Arches can form at either the northern end of the Strait, north of the Robeson Channel, or its southern end, in the vicinity of Smith Sound (Fig 1). Over the satellite record, most arches have formed at the southern terminus of the Strait[10]. There is evidence of a reduction in the duration of the arches over the past 20 years[2,10] , with several recent winters, 2006/2007, 2018/2019 and 2021/2022, during which an arch did not form. In the winter of 2016/2017, an arch collapsed early, and over the winters of 2017/2018 and 2022/2023, arches formed late in the cold season.

During the period that an arch is present, there can be a significant drop in the ice transport along the Strait[1,2,11]. Consequently, the presence or absence of an arch can have climate and ecosystem impacts beyond Nares Strait. For example, the export of sea ice along the Strait influences the salinity budget of the subpolar North Atlantic, thereby impacting the Atlantic Meridional Overturning Circulation[12]. The Arctic's largest and most productive polynya, the North Open Water (NOW) or Pikialasorsuaq (West Greenlandic for 'great upwelling'), is located south of the Strait[13]. An ice arch along the Strait contributes to its formation by blocking southward ice transport[14,15]. The high winds that flow through the narrow opening of Smith Sound also contribute to the formation of the NOW by sweeping any ice downstream[16,17]. Indeed, it has been argued that even during winters without an arch present, the winds along Smith Sound are strong enough to reduce ice cover within the NOW region[11]. The presence of an arch has, in the past, allowed migration between Inuit communities in Canada and Greenland, which has supported the transfer of technology across Nares Strait[18].

Several techniques have been used to identify arch formation. The cessation of sea ice past moorings has been employed to indicate the formation of an ice arch[8]. Visual inspection of daily infra-red imagery from the Advanced Very High Resolution Radiometer (AVHRR) flown on several polar-orbiting satellites from 1978 onward has also been used to identify the date of formation. A weakness of this approach is the need for cloud-free images to observe the sea ice[10]. A similar technique but with infra-red imagery from the Moderate Resolution Imaging Spectroradiometer (MODIS) on the Terra and Aqua polar orbiting satellites supplemented by SAR imagery from RADARSAT-1 and -2 as well as Sentinel-1A and -1B polar-orbiting satellites has also been used[9]. The ability of SAR imagery to image the surface in all-weather conditions improved the detection of arches compared to previous approaches[10].

The manual inspection of satellite imagery is both labour-intensive and involves subjectivity in decisions around the formation date related to the presence of sea ice downstream of the arch. Automatic feature tracking of sequential SAR imagery from the Envisat and RADARSAT-1 was used to calculate the ice transport across a flux gate at the northern end of Nares Strait from 1997-2010[1]. The cessation of transport across the flux gate is associated with the formation of an ice arch. A similar technique using SAR imagery from Sentinel-1A and -1B for 2016-2019 resulted in improvements due to the higher frequency of the imagery from the Sentinel satellites, usually less than a day, compared to that for the Envisat and RADARSAT satellites, typically three days. This allowed for higher temporal resolution in the ice transport and the date of arch formation. The time series has been extended[11] to January 2022 with the addition of SAR imagery from the RADARSAT Constellation Mission (RCM), thus further maintaining high temporal resolution over the Strait. Here, we further extend the time series to June 2023.

The formation of ice arches along Nares Strait results from sea ice's cohesive strength that allows it to sustain uniaxial stress as well as the narrowness of the Strait[19,20]. This strength is a function of the ice thickness, and there is concern that the observed thinning of Arctic sea ice may contribute to the reduced stability of arches along Nares Strait[1,21]. An idealized modelling study of the Smith Sound region found that stable ice arches formed with ice thicknesses on the order of 1.0 m-2.0 m with reduced cohesive strength, requiring thicker ice for arch formation[22].

Despite the important role that ice thickness plays in arch stability, remarkably little is known about its distribution along the Strait or its temporal evolution. In-situ ice thickness measurements within the Lincoln Sea, north of Nares Strait (Fig 1), indicate that during April 2017, the modal ice thickness for multi-year ice was 3.5m to 4.3m, while for first-year ice, it was approximately 2.2m [23]. Measurements from moorings within Kennedy Channel from 2003-2012 indicate a median ice draft that varied from 0.5m to 1.5m or, assuming no snow load, median ice thickness from 0.55m to 1.65m[8].

An ICESat-2 transect that crossed the ice arch in Smith Sound during January 2020 reported ice freeboards up to 0.8m[9]. Under the assumption that no snow was present, this results in a modal peak in ice thickness on the order of 2.7m[9]. Assuming 25% or 50% of the freeboard resulted from snow reduces the modal peak to approximately 2.2m or 1.6m, respectively[9]. During January 2019, a winter during which no arch formed, the ICESat-2 data indicates ice drafts on the order of 1.25m for the no snow assumption, 1.0m for the 25% snow load assumption, and 0.75m for the 50% snow load assumption[9].

This work explores the temporal and spatial variability in the merged CryoSat-2/SMOS ice thickness field along Nares Strait in the presence or absence of ice arches. This dataset provides an improved retrieval of ice thickness, especially thinner ice, with lower root mean squared errors and higher correlation as compared to in-situ observations[24]. Please refer to the Methods Section for more details on this dataset, including uncertainties.

Information on the ice area flux along Nares Strait has relied on a single flux gate situated at the northern end of Nares Strait (Figure 1). Most arches form near Smith Sound [10], so there may be a time lag between arch formation and its signal propagating upstream to affect ice transport across the northern flux gate. To assess this lag, we will also consider the transport across a southern flux gate situated within Kane Basin (Figure 1). Please refer to the Methods Section for information on ice motion and ice area flux data.

RESULTS

Table 1 provides our estimates of the formation date along with previous estimates[9,10] In general, there is agreement amongst the three estimates, with the largest discrepancy occurring during the winter of 2012/2013. Please refer to the Methods Section for a discussion as to how brightness temperatures from the 89 GHz channel on the AMSR/E and AMSR2 radiometers help resolve the date of arch formation. It should be noted that during the winter of 2022/2023, the southern arch formed on April 1. This is the latest date ever recorded for the formation of an arch[9,10].

Figure 2 characterizes the spatial variability in the ice transport along Kane Basin and Smith Sound before and after the formation of a southern ice arch on December 2, 2020. SAR imagery and associated ice motion vectors on November 30, 2020, before the formation of the arch (Figure 2a) shows southward transport along Kane Basin and Smith Sound. The magnitude of the transport is increased within the narrow confines of Smith Sound. On December 4, 2020, after the formation of the arch, there was a reduction in the magnitude of the southward transport north of the arch, while south of the arch, the transport remained large (Figure 2b). The component of ice motion normal to the southern flux gate (Figure 2c) was, before the formation of the arch, the largest in the central part of the gate. After the formation of the arch, the motion was close to zero all along the gate. The component of ice motion parallel to the centerline (Figure 2d) has a bimodal structure before and after the formation of the arch that is characterized by a local minimum in the southward transport over the southern Kane Basin. After the formation of the arch, southward ice transport continued over the northern Kane Basin.

The results presented in Figure 2 indicate that, during the winter of 2020/2021, southward ice transport continued north of the arch after its formation. In Figure 3, we present the ice area flux across the northern and southern flux gates for the four winters for which a southern arch formed during the Sentinel-1 period. As previously noted[2], the ice area flux is highly variable, and during the arch-free periods, it is, on average, positive, indicating mean southward transport. In each of the four winters, the formation of the southern arch was associated with a reduction in the ice area flux across the southern flux gate. In two winters, 2017/2018 and 2019/2020, small amplitude variability in the ice area flux across the southern flux gate remained after the formation of the arch. In the other two winters, 2020/2021 and 2022/2023, the amplitude in the ice area flux across the southern flux gate was close to zero. In all cases, the ice area flux across the northern flux gate remained large for a month or longer after the formation of the southern flux gate. In the case of the winter of 2022/2023, the ice area flux remained large across the northern gate throughout the period during which a southern arch was present (Figure 3d).

Figure 4 shows the temporal evolution of the monthly mean ice thickness along the Nares Strait centerline (Figure 1) during the winter of 2020/2021. During this winter, a southern arch formed on December 2, 2020 (Table 1). During November 2020, the thickness decreased from a maximum of ~1.8m over the Lincoln Sea to a local minimum of ~0.5m at the southern end of the

Kennedy Channel. The thickness increased over Kane Basin, reaching a local maximum of ~0.9m before decreasing to ~0.3m south of Smith Sound over northern Baffin Bay. The formation of the arch in early December 2020 led to a markedly different monthly mean ice thickness distribution. Most notable was an increase in the thickness over Kane Basin with a smaller increase in thickness over the Kennedy Channel. The arch formed just north of 79°N (Figure 2), and one can see that its formation removed the relative maximum around this location that was present in November. In subsequent months, there were continued increases in ice thickness, smaller than those in December, that were largest upstream over the Lincoln Sea, i.e. north of 83°N.

The results shown in Figure 4 suggest that during the winter of 2020/2021, an increase in thickness occurred over Kane Basin and, to a lesser extent, along Kennedy Channel in the month after the formation of a southern arch. To see if this behaviour is common to other winters during which a southern arch formed, we present in Figure 5 ice thickness distributions along the centerline for each month from January to April, composited for both those months with an arch present or absent during 2011-2023. For all months, there is a well-defined separation in the thickness distribution between the no-arch and arch composites, similar to what occurred during the winter of 2020/2021. In particular, months without an arch are characterized by a maximum ice thickness over the Lincoln Sea, a relative minimum at the southern end of Kennedy Channel, a relative maximum over Kane Basin, and a minimum south of Smith Sound over northern Baffin Bay. The presence of an arch leads to the removal of the two local extrema, resulting in a monotonic increasing ice thickness distribution with a rapid increase in thickness occurring in the vicinity of 79°N, which is associated with the presence of the arch. In addition, there tends to be an increase in thickness north of Smith Sound as the winter progresses.

We complete our presentation of results with Figure 6, which shows the spatial distribution of ice thickness during the month before and after the formation of a southern ice arch. We focus on Smith Sound and Kane Basin as this region has the largest signal (Figure 5). The local maximum over Kane Basin is evident during the month preceding arch formation (Figure 6a). After the arch forms (Figure 6b), the distribution transitions to one with a gradual increase in ice thickness north of Smith Sound. Over northern Kane Basin, the change in ice thickness after the arch forms is on the order of 0.8m.

Based on the ERA5 reanalysis[25], there were on the order of 650 freezing degree days over Kane Basin during December 2020. Based on field measurements of ice growth[26], one can estimate that, assuming no initial ice, this would have resulted in approximately 0.5m of ice growth during December 2020. Assuming that approximately 0.5 m of ice was present at the start of the month, an additional approximately 0.3m of ice growth would have occurred. This cannot account for the observed ice thickening of up to 1m, which is consistent with the idea that dynamical processes related to the convergence of ice upstream of the arch were responsible for most of the thickening that occurred in the month after arch formation. As discussed in the Methods Section, the observed change in ice thickness is also outside the range of uncertainty in CryoSat-2/SMOS retrieval of sea ice thickness.

DISCUSSION

The ice arches that form along Nares Strait and that remain stable for months at a time play an important role in the local climate and ecosystem as well as modulating the ice export from the Arctic to the subpolar North Atlantic. There is a concern that the continued thinning of Arctic sea ice may contribute to weakening the arches.

In this paper, we have examined the evolution of the ice thickness along Nares Strait in the presence or absence of a southern ice arch. In the absence of an arch, the southwards transport of ice along the Strait results in a local maximum in ice thickness to the north of Smith Sound. The convergence of ice as it encounters the narrow Smith Sound region is proposed to be the cause of this local maximum. Southern arches tend to form in this region, and this dynamical thickening is suggested to be a contributor to their formation. Immediately after the formation of the arch, there is a rapid increase in ice thickness to the north of the arch. We have shown that the southward transport of sea ice along Nares Strait continues after the formation of a southern arch. Based on the available ice motion data, this period can last over a month. We propose that the convergence of this ice as it approaches the arch is responsible for this thickening.

This work suggests that, although thinning ice is a cause for concern, the dynamics of sea ice transport along Nares Strait lead to localized thickening of sea ice that may contribute to continued arch formation. A similar suggestion was reached concerning the processes driving ice thickness north of the Canadian Arctic Archipelago[27]. Nevertheless, there is evidence that the arches are becoming less stable, as well as in recent winters when an arch did not form or formed late in the season or collapsed early. This suggests that even with ice dynamics contributing to the formation and stability of the arches along Nares Strait, changes are occurring in the region leading to their weakening, which could have profound impacts on the climate, ecosystems, and communities.

METHODS

Ice Area Flux

The ice area flux through Nares Strait was determined using an established technique [1,28,29]. First, the Komarov and Barber tracking algorithm determined sea ice motion from each sequential pair of Sentinel-1 imagery (~0.5 to 1-day time separation) [30]. Sea ice motion was then interpolated to a 30 km buffer region surrounding the gate and sampled at 5 km intervals across the gate. Two flux gates were used to calculate the ice area flux (Figure 1). The one situated at the northern end of Nares Strait is used in previous studies[2,11]. A southern flux gate within Kane Basin was also used. It was located north of the region in which southern ice arches form.

The ice area flux (F) across each gate was calculated using: $F = \sum c_i u_i \Delta x$ where c_i is the ice concentration obtained from the closest Canadian Ice Service ice chart [31] to the Sentinel-1 and RCM image date, u_i is the ice speed normal to the flux gate at the ith location and Δx is the spacing along the gate (5 km). If we assume that the errors of the sea ice motion samples are additive, unbiased, uncorrelated and normally distributed, then the uncertainty in ice area flux across the gate (σ_f) can be determined using the following equation: $\sigma_f = \sigma_e L\left(\sqrt{N_s}\right)^{-1}$, where, σ_e is the error in ice motion of 0.43 km determined previously[30], L is the width of the gate, and Ns is the number of samples across the gate. For L=139 km and Ns=27 the uncertainty in ice area flux at our gate is ~±12 km^2/day.

Date of arch formation

The formation date of ice arches along Nares Strait was determined using a combination of the ice area flux data across the southern flux gate derived from Sentinel-1A and -1B imagery, the imagery itself as well as brightness temperature data derived from the vertically polarized 89Ghz channel on the Advanced Microwave Scanning Radiometers, AMSR-E and AMSR2, on the Aqua and GCOM-W1 polar-orbiting satellites[32]. The data is available at a spatial resolution of 6.25 km. The vertically polarized 89 GHz channel has a large emissivity difference between multi-year ice, typically found north of an arch, and open water[33] that can assist in identifying an arch.

As an example, we consider the arch formation process during November 2012. As indicated in Table 1, Krillov et al.[9] quoted a formation date of November 6, 2012, while Vincent[10] quoted a date of November 8, 2012, and this study estimated that the arch formed on November 12, 2012. Figure 7 shows a sequence of the daily mean brightness temperature derived from the 89Ghz vertically polarized channel on the AMSR-E/2 radiometers[34] during November 2012. As noted by Lu et al. [35], atmospheric water vapour and cloud liquid water can impact the 89Ghz brightness temperatures over sea ice. As a result, we look for temporally invariant features in the data to identify the formation of an ice arch. No such features were present until November 12 (Figure 8b) when a region of elevated brightness temperatures can be seen near 79.25^{o}N and 72^{o}W. In this instance, we attribute the elevated brightness temperatures to the presence of open water, with warm SSTs and elevated emissivities. Over the following days (Figure 7c-f), the region of elevated brightness temperatures extends downstream with a well-defined arch at its northern end.

This development can be seen in Figure 8, which shows a Hovmöller diagram showing the brightness temperatures along the Nares Strait centerline from November 5-26, 2012. In this case, the arch formation can be seen as the right-angled triangle of elevated brightness temperatures that grows towards the south with time. The lower vertex of the triangle represents the date that the arch formed, in this case, November 12. For other winters, corresponding Hovmöller diagrams also had a similar right-angled triangle present with the lower vertex indicating the date of arch formation.

This paper focuses on the period for which ice thickness data is available, 2011-2023. Monthly mean fields are analyzed, and it is assumed that an arch is formed in a particular month if it is formed before the 15th of that month. Otherwise, it is assumed that the arch formed the following month. Before the availability of ice motion data from the Sentinel SAR imagery, we estimate the uncertainty in the formation date to be ± two days, a value consistent with that of Vincent[10] but larger than the uncertainty of ± 12 hours quoted by Krillov et al.[9]. After the availability of the ice motion data, our estimated uncertainty is reduced to ± 1 day.

Sea Ice Thickness

This paper used sea ice thickness data from the merged CryoSat-2/SMOS[24] . The dataset uses the radar altimeter on the CryoSat-2 satellite[36] as well as a 1.4 GHz passive microwave radiometer on the Moisture and Ocean Salinity (SMOS)[37]. CryoSat-2 retrievals of thin ice have a greater uncertainty as compared to thick ice, while SMOS exhibits greater sensitivity to retrievals of thin ice [24]. The merging of the two products therefore results in an improved ice thickness retrieval with lower rms errors and higher correlation compared to in-situ observations [24]. The data is available on a weekly basis, updated daily, at a spatial resolution of 25 km during the cool season (October-April) from 2010/2011 to 2022/2023[38].

Figure 9 shows the spatial distribution of the uncertainty in the CryoSat-2/SMOS ice thickness during the month before and after the formation of a southern ice arch. In both cases, uncertainties over Kane Basin are in the range of 0.3 m. The change in ice thickness before and after arch formation in this region is on the order of 0.8m. It exceeds the uncertainty, suggesting that the changes in ice thickness identified in this paper are real.

Data Availability

Sentinel-1 SAR imagery is available from the Data Space Ecosystem at: https://dataspace.copernicus.eu/. RCM SAR imagery is available from the Earth Observation Data Management System at: https://www.eodms-sgdot.nrcan-rncan.gc.ca/. The merged CyroSat-2/SMOS sea ice thickness data is available at:

https://data.seaiceportal.de/data/cs2smos_awi/v205/. The 89Ghz brightness temperature data is available from the National Snow and Ice Data Center https://nsidc.org/data/au_si6/versions/1.

REFERENCES

1 Kwok, R., Toudal Pedersen, L., Gudmandsen, P. & Pang, S. S. Large sea ice outflow into the Nares Strait in 2007. *Geophysical Research Letters* **37**, n/a-n/a, doi:10.1029/2009GL041872 (2010).

2 Moore, G., Howell, S., Brady, M., Xu, X. & McNeil, K. Anomalous collapses of Nares Strait ice arches leads to enhanced export of Arctic sea ice. *Nature communications* **12**, 1-8 (2021).

3 Howell, S. *et al.* A comparison of Arctic Ocean sea ice export between Nares Strait and the Canadian Arctic Archipelago. *Journal of Geophysical Research: Oceans*, e2023JC019687 (2023).

4 Smedsrud, L. H., Halvorsen, M. H., Stroeve, J. C., Zhang, R. & Kloster, K. Fram Strait sea ice export variability and September Arctic sea ice extent over the last 80 years. *The Cryosphere* **11**, 65-79 (2017).

5 Münchow, A. Volume and freshwater flux observations from Nares Strait to the west of Greenland at daily time scales from 2003 to 2009. *Journal of Physical Oceanography* **46**, 141-157 (2016).

6 Moore, G. W. K., Schweiger, A., Zhang, J. & Steele, M. Spatiotemporal Variability of Sea Ice in the Arctic's Last Ice Area. *Geophysical Research Letters* (2019).

7 Stroeve, J. & Notz, D. Changing state of Arctic sea ice across all seasons. *Environmental Research Letters* **13**, 103001 (2018).

8 Ryan, P. A. & Münchow, A. Sea ice draft observations in N ares S trait from 2003 to 2012. *Journal of Geophysical Research: Oceans* **122**, 3057-3080 (2017).

9 Kirillov, S. *et al.* On the physical settings of ice bridge formation in Nares Strait. *Journal of Geophysical Research: Oceans* **126**, e2021JC017331 (2021).

10 Vincent, R. A study of the north water polynya ice arch using four decades of satellite data. *Scientific Reports* **9**, 1-12 (2019).

11 Moore, G., Howell, S. & Brady, M. Evolving relationship of Nares Strait ice arches on sea ice along the Strait and the North Water, the Arctic's most productive polynya. *Scientific Reports* **13**, 9809 (2023).

12 Sévellec, F., Fedorov, A. V. & Liu, W. Arctic sea-ice decline weakens the Atlantic meridional overturning circulation. *Nature Climate Change* **7**, 604-610 (2017).

13 Barber, D. G. & Massom, R. A. in *Elsevier Oceanography Series* Vol. 74 (eds W. O. Smith & D. G. Barber) 1-54 (Elsevier, 2007).

14 Barber, D. G., Hanesiak, J. M., Chan, W. & Piwowar, J. Sea-ice and meteorological conditions in Northern Baffin Bay and the North Water polynya between 1979 and 1996. *Atmosphere-Ocean* **39**, 343-359, doi:10.1080/07055900.2001.9649685 (2001).

15 Melling, H., Gratton, Y. & Ingram, G. Ocean circulation within the North Water polynya of Baffin Bay. *Atmosphere-Ocean* **39**, 301-325 (2001).

16 Ito, H. Wind through a channel—Surface wind measurements in Smith Sound and Jones Sound in northern Baffin Bay. *Journal of Applied Meteorology and Climatology* **21**, 1053-1062 (1982).

17 Moore, G. W. K. & Imrit, A. A. Impact of Resolution on the Representation of the Mean and Extreme Winds along Nares Strait. *Journal of Geophysical Research: Atmospheres*, doi:https://doi.org/10.1029/2022JD037443 (2022).

18 Pikialasorsuaq_Commission. People of the Ice Bridge: the future of the Pikialasorsuaq. (2017).

19 Hibler, W., Hutchings, J. & Ip, C. Sea-ice arching and multiple flow states of Arctic pack ice. *Annals of Glaciology* **44**, 339-344 (2006).

20 Rallabandi, B., Zheng, Z., Winton, M. & Stone, H. A. Formation of sea ice bridges in narrow straits in response to wind and water stresses. *Journal of Geophysical Research: Oceans* **122**, 5588-5610, doi:10.1002/2017JC012822 (2017).

21 Moore, G. W. K. & McNeil, K. The Early Collapse of the 2017 Lincoln Sea Ice Arch in Response to Anomalous Sea Ice and Wind Forcing. *Geophysical Research Letters* **45**, 8343-8351, doi:10.1029/2018GL078428 (2018).

22 Dumont, D., Gratton, Y. & Arbetter, T. E. Modeling the dynamics of the North Water polynya ice bridge. *Journal of Physical Oceanography* **39**, 1448-1461 (2009).

23 Haas, C. *et al.* Ice and snow thickness variability and change in the high Arctic Ocean observed by in situ measurements. *Geophysical Research Letters* **44**, 10,462-410,469 (2017).

24 Kaleschke, L. *et al.* in *2015 IEEE International Geoscience and Remote Sensing Symposium (IGARSS).* 5232-5235 (IEEE).

25 Hersbach, H. *et al.* The ERA5 global reanalysis. *Quarterly Journal of the Royal Meteorological Society* **146**, 1999-2049 (2020).

26 Maykut, G. A. in *The geophysics of sea ice* (ed N. Untersteiner) 395-463 (Springer, 1986).

27 Melling, H. Thickness of multi-year sea ice on the northern Canadian polar shelf: a second look after 40 years. *The Cryosphere* **16**, 3181-3197 (2022).

28 Howell, S. E. *et al.* Recent changes in the exchange of sea ice between the Arctic Ocean and the Canadian Arctic Archipelago. *Journal of Geophysical Research: Oceans* **118**, 3595-3607 (2013).

29 Kwok, R. Exchange of sea ice between the Arctic Ocean and the Canadian Arctic Archipelago. *Geophysical Research Letters* **33** (2006).

30 Komarov, A. S. & Barber, D. G. Sea ice motion tracking from sequential dual-polarization RADARSAT-2 images. *IEEE Transactions on Geoscience and Remote Sensing* **52**, 121-136 (2013).

31 Tivy, A. *et al.* Trends and variability in summer sea ice cover in the Canadian Arctic based on the Canadian Ice Service Digital Archive, 1960–2008 and 1968–2008. *Journal of Geophysical Research: Oceans* **116** (2011).

32 Comiso, J. C., Cavalieri, D. J. & Markus, T. Sea ice concentration, ice temperature, and snow depth using AMSR-E data. *IEEE Transactions on Geoscience and Remote Sensing* **41**, 243-252, doi:10.1109/TGRS.2002.808317 (2003).

33 Spreen, G., Kaleschke, L. & Heygster, G. Sea ice remote sensing using AMSR-E 89-GHz channels. *Journal of Geophysical Research: Oceans* **113** (2008).

34 Meier, W., Comiso, J. & Markus, T. (NASA National Snow and Ice Data Center Distributed Active Archive Center. , 2018).

35 Lu, J., Scarlat, R., Heygster, G. & Spreen, G. Reducing Weather Influences on an 89 GHz Sea Ice Concentration Algorithm in the Arctic Using Retrievals From an Optimal Estimation Method. *Journal of Geophysical Research: Oceans* **127**, e2019JC015912, doi:https://doi.org/10.1029/2019JC015912 (2022).

36 Wingham, D. *et al.* CryoSat: A mission to determine the fluctuations in Earth's land and marine ice fields. *Advances in Space Research* **37**, 841-871 (2006).

37 Kerr, Y. H. *et al.* Soil moisture retrieval from space: the Soil Moisture and Ocean Salinity (SMOS) mission. *IEEE Transactions on Geoscience and Remote Sensing* **39**, 1729-1735, doi:10.1109/36.942551 (2001).

38 Hendricks, S., Ricker, R. & Paul, S. Product User Guide & Algorithm Specification: AWI CryoSat-2 Sea Ice Thickness (version 2.4). (2021).

ACKNOWLEDGEMENTS

The authors would like to thank the Copernicus Programme of the European Space Agency for access to the Sentinel-1 SAR imagery. All figures were created by the authors using the MATLAB software system. GWKM would like to acknowledge funding support from the Natural Sciences and Engineering Research Council of Canada.

AUTHOR CONTRIBUTIONS

GWKM conceived the study. SELH and MB analyzed the SAR imagery and generated the ice motion data. GWKM, SELH, TB, KMc and MB contributed to the analysis and the writing of the manuscript.

COMPETING INTERESTS

The authors declare no competing interests.

FIGURE CAPTIONS

Figure 1) Topography (km) of the Nares Strait region as represented in the GEBCO Digital Elevation Model. The abbreviations for locations along the Strait are northern Baffin Bay (NBB), Smith Sound (SS), Kane Basin (KB), Kennedy Channel (KC), Robeson Channel (RC), and the Lincoln Sea (LS). The thick red and blue lines indicate the location of the northern (red) and southern (blue) flux gates used to characterize ice motion along Nares Strait. The dotted black curve represents the centerline of Nares Strait.

Figure 2) Variability of the ice motion in Kane Basin and Smith Sound. Ice motion (km/d) and S1 SAR satellite imagery on: a) November 30 2020 (before the formation of the southern arch) and b) December 4 2020 (after the formation of the southern arch) with the southern flux gate indicated by the blue line and the centerline indicated by the magenta curve. The : c) normal component of ice motion (positive southwards)across the southern flux gate and d) parallel component of ice motion (positive southwards) along the centerline before (red) and after (blue) the arch formation that occurred on Dec 2, 2020.

Figure 3) Time series of the ice area flux (103km2/day) across the Nares Strait northern (black) and southern (red) flux gates. Results are shown for the winters of: a) 2017/2018, b) 2019/2020, c) 2020/2021, and d) 2022/2023. The dates of arch formation are indicated by the vertical dashed lines. Southward ice area fluxes are positive.

Figure 4) Spatial evolution of the monthly mean ice thickness along the Nares Strait centerline. Results are shown for the months of November through April for the winter of 2020/2021. All months are labelled with respect to the presence of absence of an arch. All data from the AWI CryoSat2-SMOS dataset.

Figure 5) Spatial evolution of the ice thickness along the Nares Strait centerline. Results are shown during winters 2010/2011 to 2022/2023 for: a) January, b) February, c) March, and d)April.

The red curves are the medians for years in which an arch was present during the respective months with the light red shading encompassing thicknesses bounded by the 25% and 75% percentiles. The blue curves and light blue shading correspond to years in which an arch was not present. All data from the AWI Cryosat2-SMOS dataset 2011-2023.

Figure 6) Spatial distribution of the ice thickness (m) along Smith Sound and Kane Basin. Results are shown for the months: a) preceding and b) following the formation of a southern arch. The centerline is indicated by the blue line. All data from the AWI Cryosat2-SMOS dataset 2011-2023.

Figure 7) Brightness temperature (K) based on the AMSR2 vertically polarized 89Ghz channel for: a) November 6, 2012; b) November 12, 2012; c) November 15, 2012; d) November 20, 2012; e) November 25, 2012; and f) November 30, 2012. The centerline is indicated by the black line.

Figure 8) Hovmöller diagram of the brightness temperature (K) based on the AMSR2 vertically polarized 89Ghz channel along the Nares Strait centerline for the period November 1-29 2012.

Figure 9) Spatial distribution of uncertainty in the ice thickness (m) along Smith Sound and Kane Basin. Results are shown for the months: a) preceding and b) following the formation of a southern arch. The centerline is indicated by the blue line. All data from the AWI Cryosat2-SMOS dataset 2011-2023.

Winter	This Study	Krillov et al. (2021)	Vincent (2019)
2010/2011	January 31, 2011 ± 2 days	January 29, 2011	January 31, 2011
2011/2012	December 05, 2011 ± 2 days	December 05, 2011	December 06, 2011
2012/2013	November 12, 2012 ± 2 days	November 06, 2012	November 08, 2012
2013/2014	January 11, 2014 ± 2 days	January 08, 2014	January 15, 2014
2014/2015	February 16, 2015 ± 2 days	February 11, 2015	February 14, 2015
2015/2016	December 07, 2015 ± 2 days	December 05, 2015	December 05,2015
2016/2017	*No southern arch*	*No southern arch*	*No southern arch*
2017/2018	March 1, 2018 ± 1 day	February 27, 2018	March 04, 2018
2018/2019	*No arches*	*No arches*	*No arches*
2019/2020	December 17, 2019 ± 1 day	December 17, 2019	
2020/2021	December 02, 2020 ± 1 day	December 04, 2020	
2021/2022	*No arches*		
2022/2023	April 01, 2023 ± 1 day		

Table 1 Formation date for southern Nares Strait arches 2010-2023

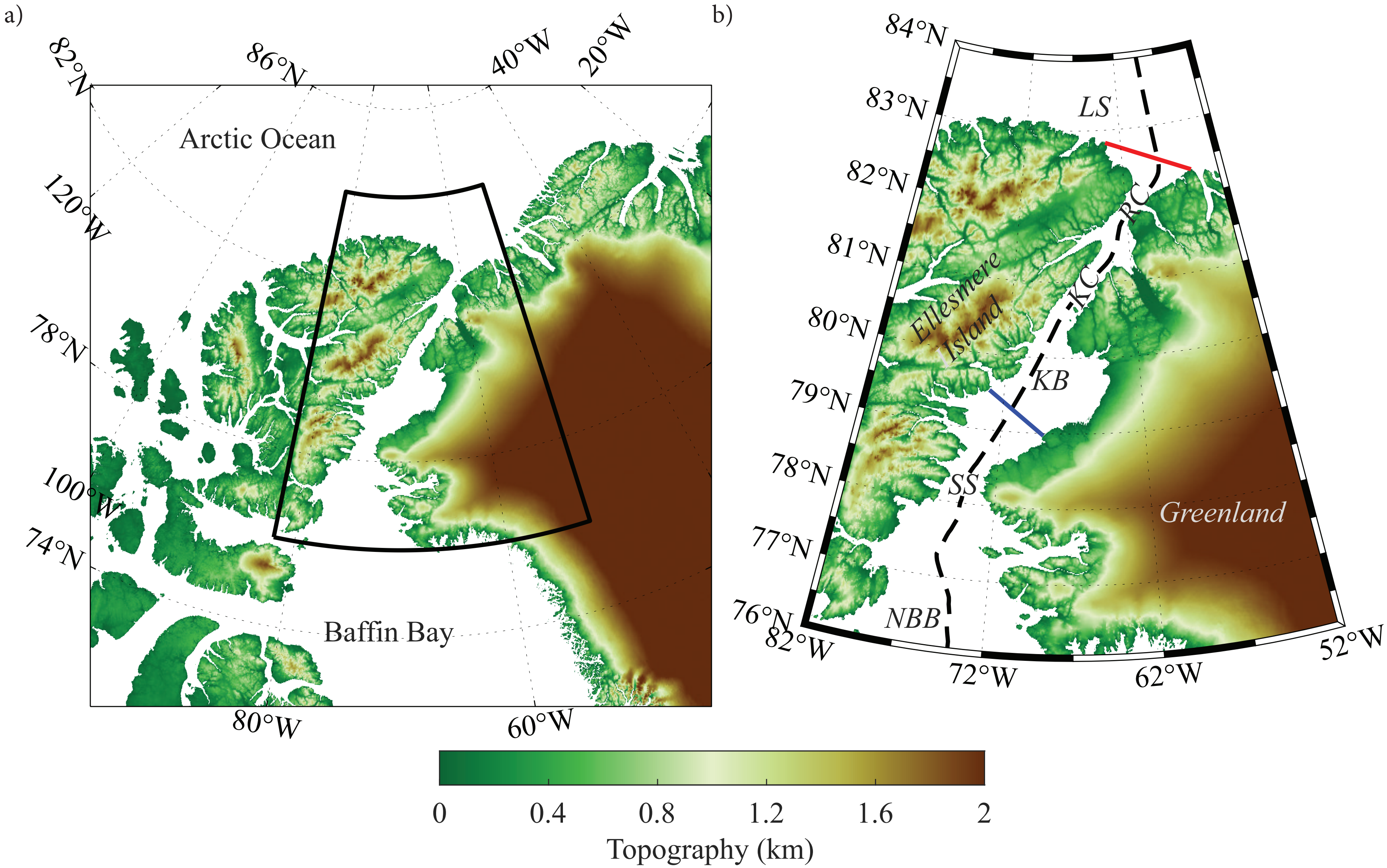

Figure 1) Topography (km) of the Nares Strait region as represented in the GEBCO Digital Elevation Model. The abbreviations for locations along the Strait are northern Baffin Bay (NBB), Smith Sound (SS), Kane Basin (KB), Kennedy Channel (KC), Robeson Channel (RC), and the Lincoln Sea (LS). The thick red and blue lines indicate the location of the northern (red) and southern (blue) flux gates used to characterize ice motion along Nares Strait. The dotted black curve represents the centerline of Nares Strait.

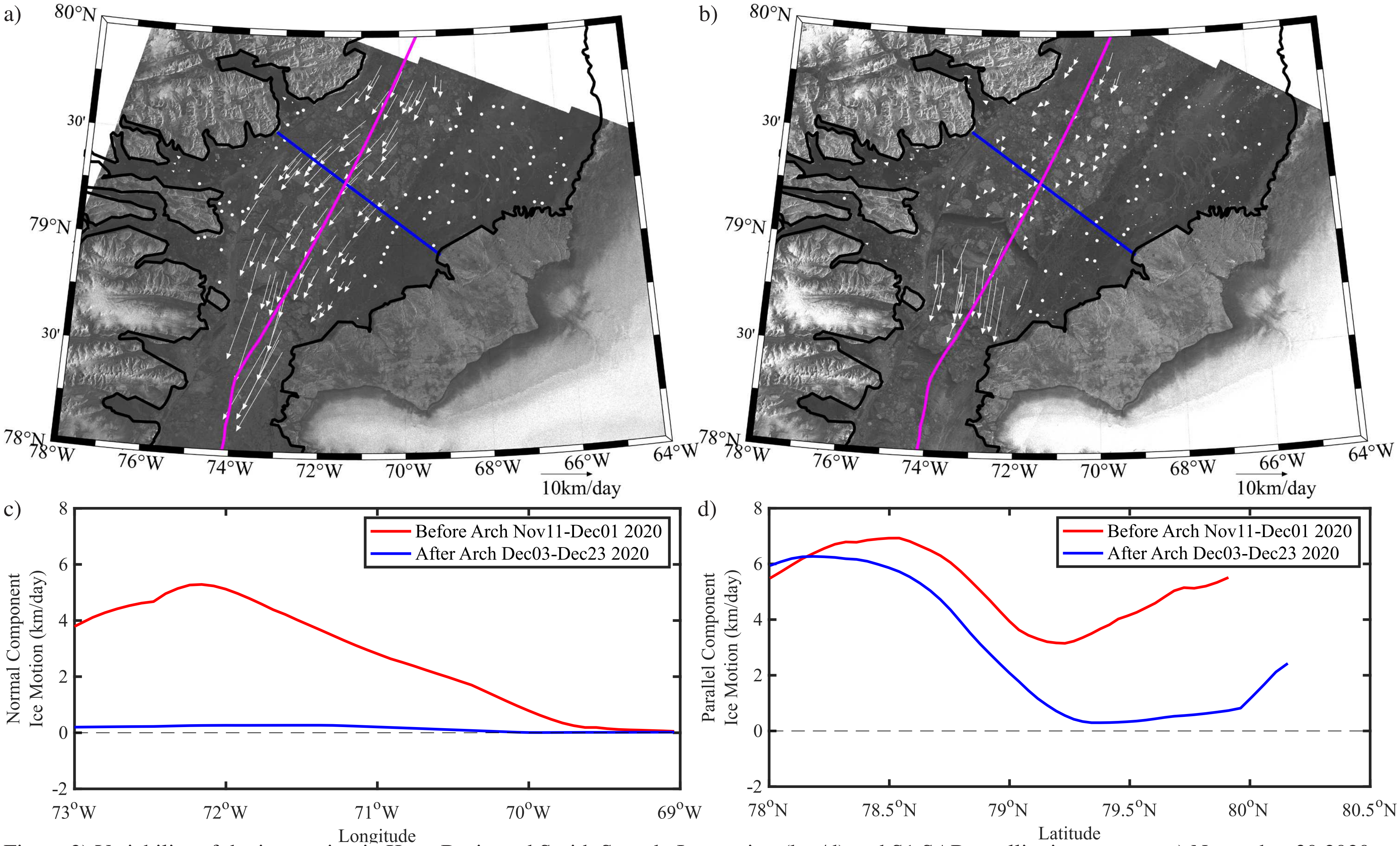

Figure 2) Variability of the ice motion in Kane Basin and Smith Sound. Ice motion (km/d) and S1 SAR satellite imagery on: a) November 30 2020 (before the formation of the southern arch) and b) December 4 2020 (after the formation of the southern arch) with the southern flux gate indicated by the blue line and the centerline indicated by the magenta curve. The: c) normal component of ice motion (positive southwards) across the southern flux gate and d) parallel component of ice motion (positive southwards) along the centerline before (red) and after (blue) the arch formation that occurred on Dec 2, 2020.

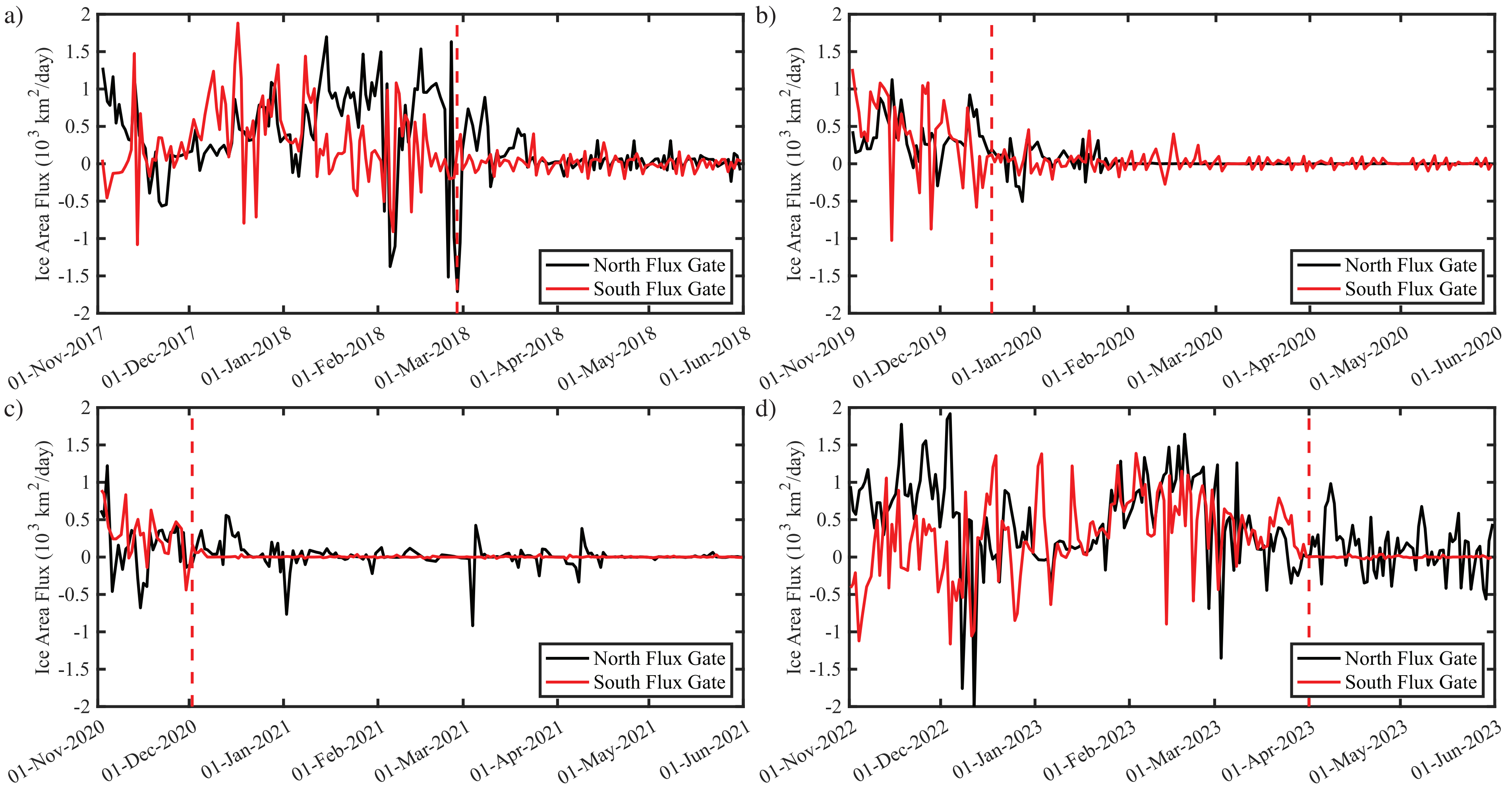

Figure 3) Time series of the ice area flux (10^3km^2/day) across the Nares Strait northern (black) and southern (red) flux gates. Results are shown for the winters of: a) 2017/2018, b) 2019/2020, c) 2020/2021, and d) 2022/2023. The dates of arch formation are indicated by the vertical dashed lines. Southward ice area fluxes are positive.

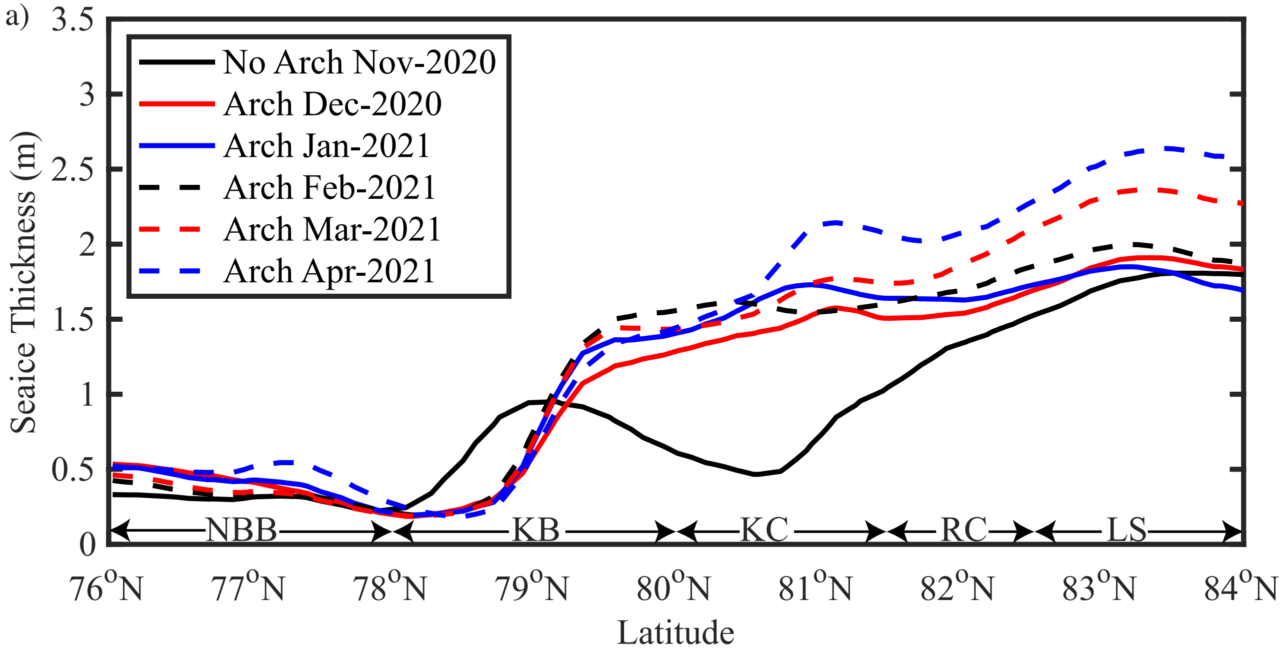

Figure 4) Spatial evolution of the monthly mean ice thickness along the Nares Strait centerline. Results are shown for the months of November through April for the winter of 2020/2021. All months are labelled with respect to the presence of absence of an arch. The locations of the Northern Baffin Bay (NBB), Kane Basin (KB), Kennedy Channel (KC), Robeson Channel (RC) and Lincoln Sea (LS) are indicated. All data from the AWI CryoSat2-SMOS dataset.

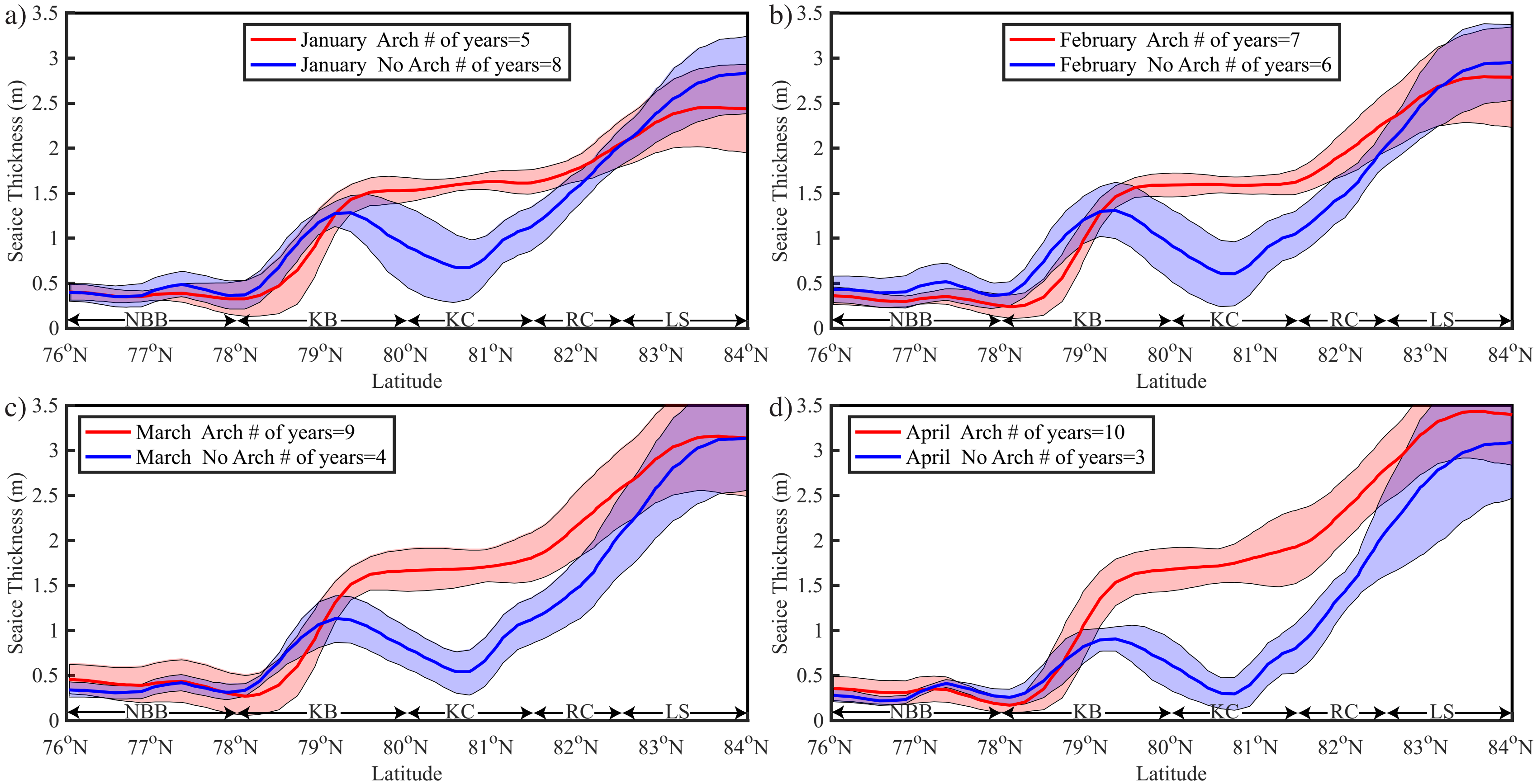

Figure 5) Spatial evolution of the ice thickness along the Nares Strait centerline. Results are shown during winters 2010/2011 to 2022/2023 for: a) January, b) February, c) March, and d)April. The red curves are the medians for years in which an arch was present during the respective months with the light red shading encompassing thicknesses bounded by the 25% and 75% percentiles. The blue curves and light blue shading correspond to years in which an arch was not present. The locations of the Northern Baffin Bay (NBB), Kane Basin (KB), Kennedy Channel (KC), Robeson Channel (RC) and Lincoln Sea (LS) are indicated. All data from the AWI CryoSat2-SMOS dataset.

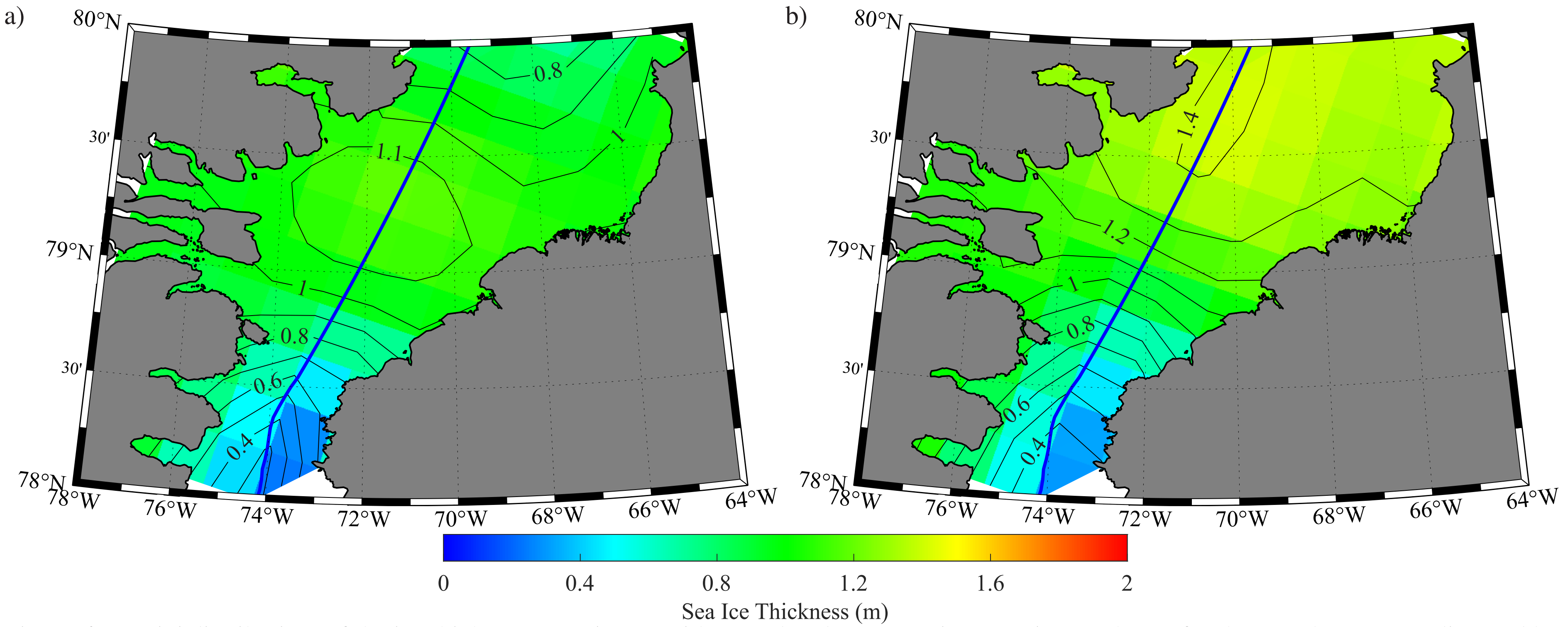

Figure 6) Spatial distribution of the ice thickness (m) along Smith Sound and Kane Basin. Results are shown for the months: a) preceding and b) following the formation of a southern arch. The centerline is indicated by the blue line. All data from the AWI Cryosat2-SMOS dataset 2011-2023.

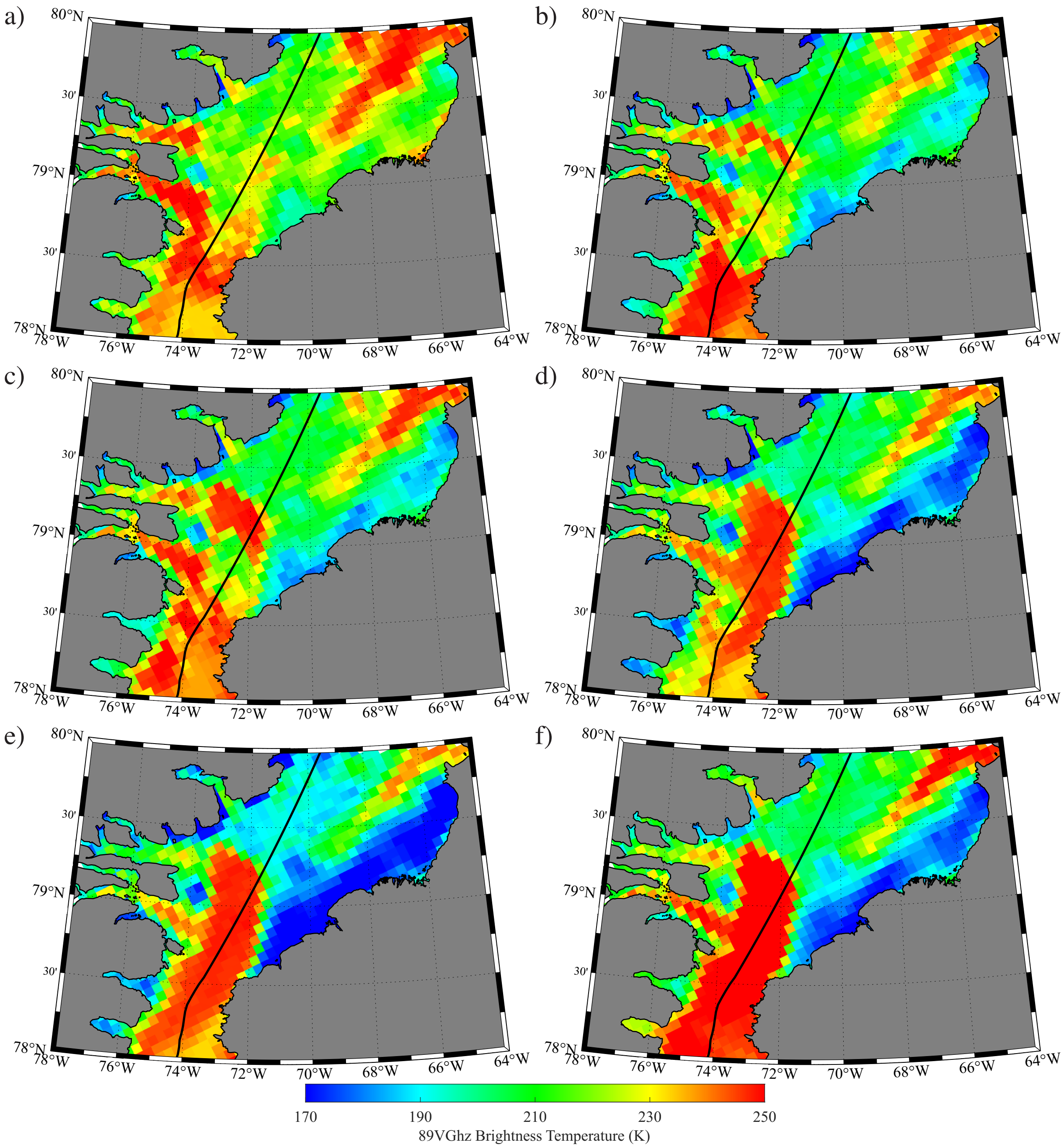

Figure 7) Brightness temperature (K) based on the AMSR2 vertically polarized 89Ghz channel for: a) November 6, 2012; b) November 12, 2012; c) November 15, 2012; d) November 20, 2012; e) November 25, 2012; and f) November 30, 2012. The centerline is indicated by the black line.

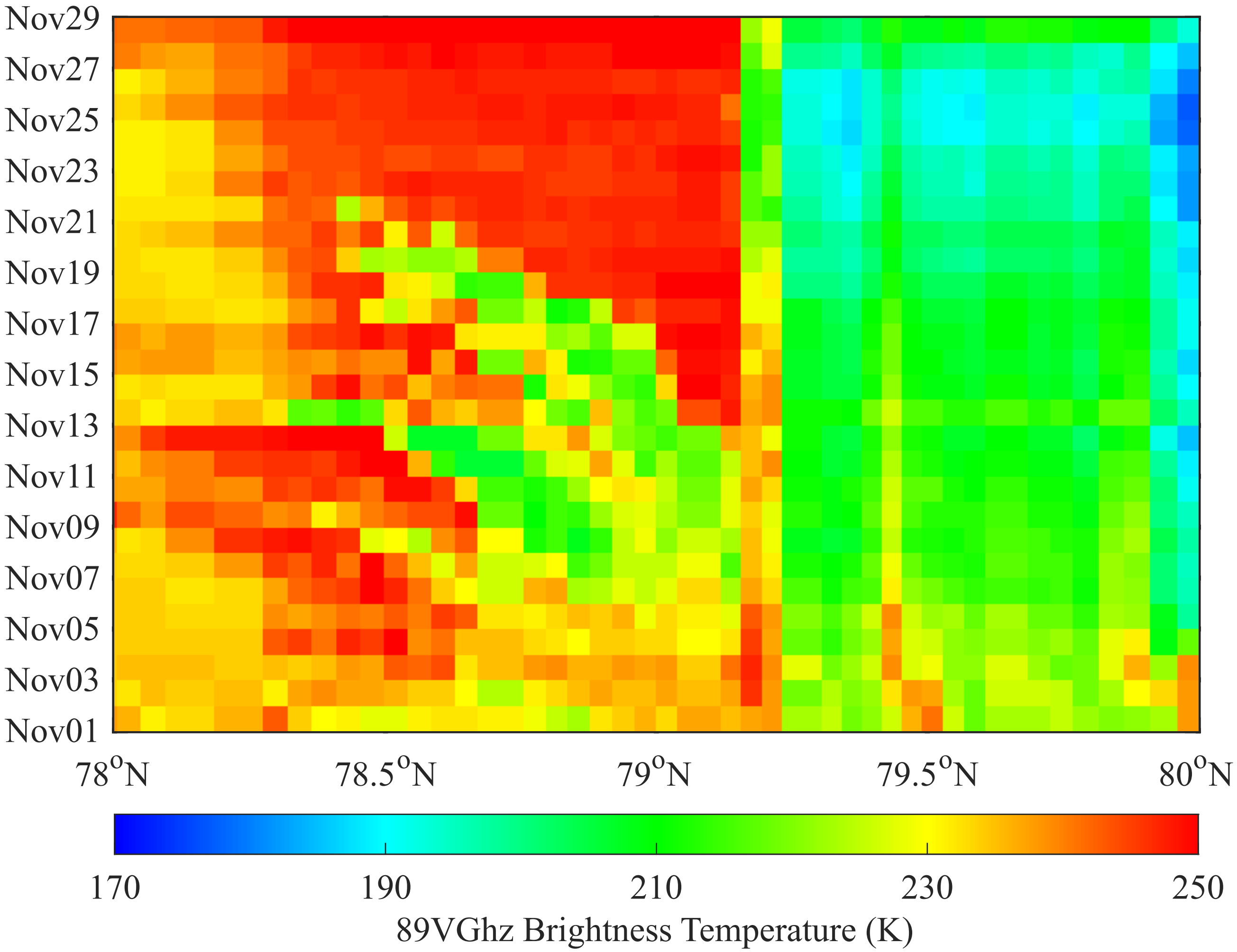

Figure 8) Hovmöller diagram of the brightness temperature (K) based on the AMSR2 vertically polarized 89Ghz channel along the Nares Strait centerline for the period November 1-29 2012.

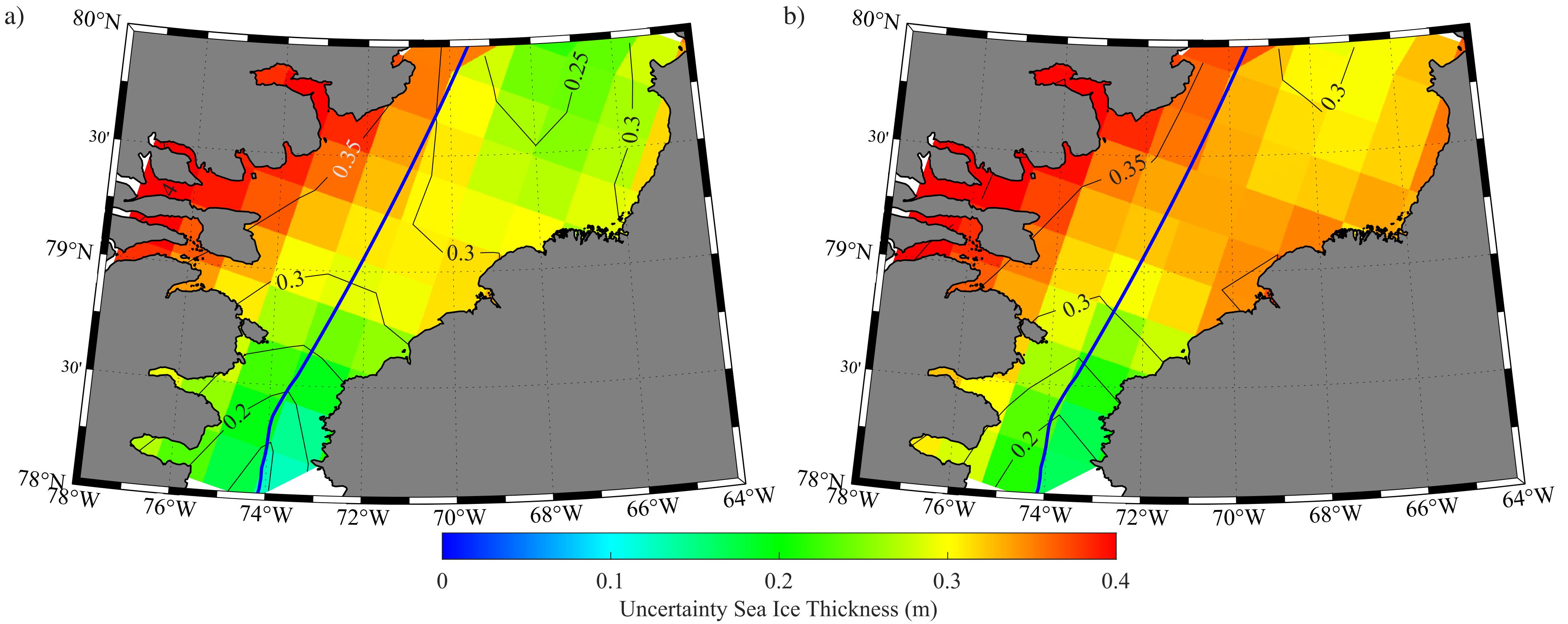

Figure 9) Spatial distribution of uncertainty in the ice thickness (m) along Smith Sound and Kane Basin. Results are shown for the months: a) preceding and b) following the formation of a southern arch. The centerline is indicated by the blue line. All data from the AWI Cryosat2-SMOS dataset 2011-2023.